Received: 3 February 2023 | Revised: 21 April 2023 | Accepted: 21 April 2023

DOI: 10.1002/jbio.202300035

RESEARCH ARTICLE

JOURNAL OF BIOPHOTONICS

# Implementation of data fusion to increase the efficiency of classification of precancerous skin states using in vivo bimodal spectroscopic technique

**Valentin Kupriyanov**[1,2] | **Walter Blondel**[1] | **Christian Daul**[1] | **Marine Amouroux**[1] | **Yury Kistenev**[2,3]

[1]Université de Lorraine, CNRS, CRAN UMR 7039, Nancy, France

[2]Laboratory of Laser Molecular Imaging and Machine Learning, Tomsk State University, Tomsk, Russia

[3]Laboratory for Remote Sensing of the Environment, V.E. Zuev Institute of Atmospheric Optics SB RAS, Tomsk, Russia

**Correspondence**
Valentin Kupriyanov, Université de Lorraine, CNRS, CRAN UMR 7039, F-54000 Nancy, France.
Email: valentin.kupriyanov@univ-lorraine.fr

**Funding information**
French Government; Russian Government; Université de Lorraine

**Abstract**

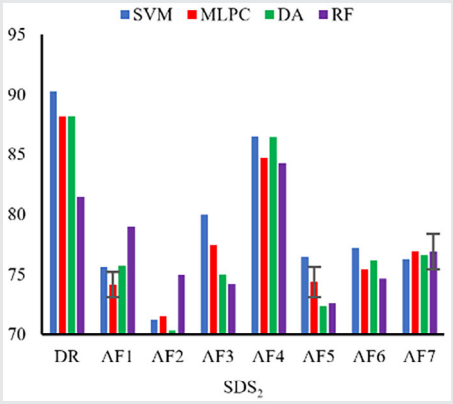


This study presents the results of the classification of diffuse reflectance (DR) spectra and multiexcitation autofluorescence (AF) spectra that were collected in vivo from precancerous and benign skin lesions at three different source detector separation (SDS) values. Spectra processing pipeline consisted of dimensionality reduction, which was performed using principal component analysis (PCA), followed by classification step using such methods as support vector machine (SVM), multilayered perceptron (MLP), linear discriminant analysis (LDA), and random forest (RF). In order to increase the efficiency of lesion classification, several data fusion methods were applied to the classification results: majority voting, stacking, and manual optimization of weights. The results of the study showed that in most of cases the use of data fusion methods increased the average multiclass classification accuracy from 2% up to 4%. The highest accuracy of multiclass classification was obtained using the manual optimization of weights and reached 94.41%.

**KEYWORDS**

autofluorescence, data fusion, diffuse reflectance, machine learning, multimodal spectroscopic method, skin cancer

**Abbreviations:** AF, autofluorescence; AH, atypical hyperplasia; CH, compensatory hyperplasia; CV, cross-validation; D, dysplasia; DR, diffuse reflectance; H, healthy; KNN, k-nearest neighbors; LDA, linear discriminant analysis; LOOCV, leave-one-out cross validation; MO, manual optimization of weights; MV, majority voting; OVO, one versus one; OVR, one versus rest; PCA, principal component analysis; PP, potentially precancerous (skin state); RBF, radial based function; SDS, source-detector separation; SVM, support vector machine.

## 1 | INTRODUCTION

The standard clinical procedure for skin cancer diagnosis in case of a suspicious lesion is based on a surgical biopsy for histopathological grading. But this procedure is invasive and has low sensitivity: Heal et al. [1] showed that

  

the diagnosis of skin cancer and precancerous skin states using conventional biopsy was associated with a sensitivity of 63.9% for basal cell carcinoma, 41.1% for squamous cell carcinoma, and 33.8% for malignant melanomas.

In recent years, noninvasive optical methods of skin cancer diagnosis using optical technology including optical coherence tomography [2–4], confocal microscopy [5–7], hyperspectral [8–10], and multispectral imaging [11, 12], spectroscopic methods such as Raman spectroscopy [13–16], autofluorescence (AF) spectroscopy [17–19], and diffuse reflectance (DR) spectroscopy [20–22], have been actively developed. The most common advantages of these methods, referred to as optical biopsy [23, 24], are noninvasiveness and the ability to perform the examination in real time. However, all of these methods deal with one or several physical properties of the skin under study, which may not always be sufficient for differential diagnosis of states with close symptoms.

A very promising approach is to combine several techniques in a single study to improve diagnostic accuracy. Among these combined systems, which are also referred to as multimodal, a combination of AF spectroscopy and DR spectroscopy is most often [24–28], as it provides the information on both endogenous fluorophore concentrations (by AF spectra) and skin absorption and scattering properties (by DR spectra). These methods can also be easily combined in one device. DR and mono-AF spectroscopy can be also combined with Raman spectroscopy [29, 30]. To summarize, DR and AF spectroscopy provides a significant amount of information for the diagnosis of skin lesions and can be easily in combined in one device.

Despite all advantages, application of the combination of AF and DR spectroscopy for skin analysis requires the use of data processing methods for feature extraction/selection and classification, as the absorption and fluorescence ranges of the skin internal components have many overlaps in the visible range, which significantly complicates analysis and interpretation of results. Statistical methods [31, 32] and principal component analysis (PCA) [33, 34] are most commonly used for feature selection/extraction. For spectrum classification purposes, SVM [32, 34], LDA [35], and artificial neural networks [36–38] are the most commonly used.

Implementation of bimodal spectroscopic device for diagnosis of benign and precancerous skin states were investigated by our team in several studies. In Ref. [39], a combination of AF spectroscopy and DR spectroscopy in a bimodal approach improves the accuracy of pairwise classification between the four histological classes of mouse skin carcinogenesis compared to each modality used separately. In a second published study [40], our team showed that the use of multiple SDSs improves diagnostic accuracy and that SVM was the most appropriate classification algorithm compared with LDA and k-nearest neighbors (KNN) for our task. Classification was also performed pairwise for all classes. In the previous study [41], a hybrid feature selection approach (discrete cosine transform and mutual information) was applied. Classification was also performed by using SVM one versus all method. The obtained accuracy of the multiclass classification was 81.7%. However, the obtained value is lower than for traditional biopsy and should be increased.

A possible way to increase the accuracy of classification of data obtained from different sources is the use of voting or data fusion methods [42]. In context of combining initial data for further implementation of machine learning methods, all the data fusion methods can be roughly divided into three types: fusion of the data before processing, decision fusion methods, and methods that combine both strategies. In previous studies [39–41], our team tested only the first type of data fusion, however, implementation of other strategies, such as decision fusion, is rather promising.

The aim of this study is to develop and optimize a DR and multiexcitation AF spectra analysis pipeline, including dimensionality reduction, classification and application of various data fusion techniques to properly combine information obtained by different groups of spectra. We propose to use PCA to reduce the dimensionality of the spectra without extracting spectral features. Support vector machine, linear discriminant analysis, multilayer perceptron classifier, and random forest classifier were chosen for classification step, followed by a data fusion step using majority voting, stacking, and manual optimization of weights for the results of classification.

The paper is organized as follows. In Section 2, it describes the data set under study, the experimental setup and the data analysis methods that were used in the study. The results of lesion classification before and after the application of data fusion methods are shown in Section 3.

## 2 | MATERIALS AND METHODS

### 2.1 | Experimental setup

A detailed description of the multimodal spatially resolved spectroscopic system used in the study was presented in the previous papers [39–41]. The main scheme of this set-up is shown in Figure 1.

Xenon lamp emitting mainly in the 300–800 nm spectral range and a system of linearly variable band-pass filters were used to obtain multiexcitation AF and DR

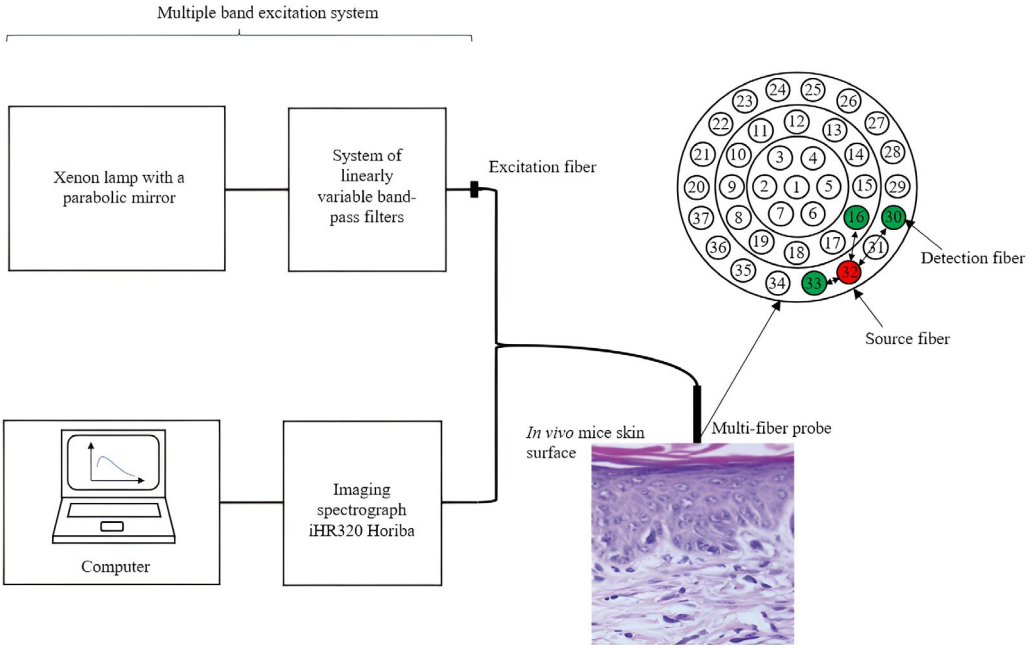


**FIGURE 1** Scheme of the spectroscopic set-up.

**TABLE 1** Main light source and detection characteristics of the device used during the experimental study.

| Modality | Source wavelength (nm) | Output power (μW) | Spectra acquisition range (nm) | Source-detector separations (μm) |
|---|---|---|---|---|
| Diffuse reflectance spectroscopy | Ranges | | | |
| | 370–540 | 430 | | |
| | 450–640 | 305 | | |
| | 560–740 | 242 | | |
| Multiexcitation Autofluorescence spectroscopy | Peak (FWHM) | | | |
| | $AF_1 = 360$ (17) | 19 | 390–720 | $SDS_1 = 271$ |
| | $AF_2 = 368$ (17) | 25 | | $SDS_2 = 536$ |
| | $AF_3 = 390$ (17) | 32 | | $SDS_3 = 834$ |
| | $AF_4 = 400$ (15) | 30 | | |
| | $AF_5 = 410$ (15) | 30 | | |
| | $AF_6 = 420$ (15) | 26 | | |
| | $AF_7 = 430$ (15) | 20 | | |

*Abbreviation*: FWHM, full width at half maximum.

spectra corresponding to different excitation wavelengths or DR spectra. The light was focused into the source fiber core, that contains 37 optical fibers (numerical aperture is 0.22, SEDI, France) arranged in concentric circles within the 2 mm-diameter bundle. For this application, three different source-detector separations were selected: 271 μm ($SDS_1$), 536 μm ($SDS_2$), and 834 μm ($SDS_3$) for distances between the excitation fiber #32 and the detection fibers #33, #16 and #30, respectively (see Figure 1). The latter were selected among the bundle fibers as close as possible to the probe border in order to be more easily located by the investigator and precisely positioned onto the skin measurement area targeted. Main characteristics of the device are shown in Table 1, including AF excitation peak wavelengths and average output (incident) power used during the study.

The spectra collected at three SDS were simultaneously measured by an imaging spectrograph. Each measure was repeated three times and then averaged to improve the signal-to-noise ratio. These averaged spectra were used as the initial data for further processing.

TABLE 2 Main characteristics of the initial dataset.

| Class | Label | Prognosis | Number of samples |
|---|---|---|---|
| Healthy | H | Not at risk | 84 |
| Compensatory hyperplasia | CH | Not at risk | 47 |
| Atypically hyperplasia | AH | Potentially precancerous | 59 |
| Dysplasia | D | Potentially precancerous | 56 |
| | | Total | 246 |

## 2.2 | Characteristics of the dataset under study

The experimental protocol of this study was approved by the French Ethical Committee on Animal Experimentation. Twelve-week-old female mice were divided into two groups: the control group with eight sham-irradiated mice and the test group included 20 mice, that were irradiated by UV with a fluence of 3 mW/cm$^2$ for 20 s each time from the dorsal side [40]. Spectra were collected on the backs of mice at several constant points to increase the chance of reaching the lesions.

The data set consisted of AF and DR spectra measured in vivo on $N = 246$ mice skin samples. Based on the results of the histopathological analysis, all mouse skin samples were classified into four classes: healthy skin (H), compensatory hyperplasia (CH), atypical hyperplasia (AH), and dysplasia (D).

It should be noted that atypical hyperplasia presents the risk of evolving into dysplasia, which in turn can develop into benign neoplasia or squamous cell carcinoma. Whereas compensatory hyperplasia is not a precancerous state of skin. Therefore, classifying all the spectra as potentially precancerous (PP) and not at risk is also of some interest. The characteristics of the data set under study are presented in Table 2.

Compensatory hyperplasia is characterized by the proliferation of keratinocytes, so mitoses can be detected in the upper layers, whereas "normally" they are limited to the basal layer. Hyperproliferation is accompanied by strong metabolic activity of keratinocytes, which leads to increased keratin synthesis, as a result of which the keratin layer covering the epidermis increases significantly.

Atypical hyperplasia corresponds to the "intermediate" state of the tissue, that is, the stage when abnormal morphological elements become visually distinguishable, but no accumulations were detected. Among the abnormal effects, chromatin heterogeneity in the nuclei was mainly distinguished, with the upper layers still containing nuclei, which indicates cytological dismaturation and disorganization of cell layers.

In case of dysplastic hyperplasia (or "dysplasia") in addition to the presence of atypical cells mentioned before, there were characteristic features of keratinocyte dysfunction (parakeratosis and dyskeratosis) and dermal fibroblasts (elastosis). Parakeratosis corresponds to a keratin layer that still contains keratinocytes or cell nuclei, whereas normally the stratum corneum consists only of fully mature keratin filaments. Dyskeratoses correspond to fully mature (differentiated) keratinocytes in the lower layers, whereas normally keratinocytes fully mature only on the surface, in the stratum corneum. Similarly, fibroblasts of the dermis damaged by UV radiation synthesize abnormal elastic fibers: short and thick. Thus, atypical hyperplasia and dysplasia have similar symptoms and have similar effects mostly on the morphology of the tissue and, as a consequence, on its scattering properties. However, the effect of dysplasia on skin properties is stronger.

The main symptoms of the skin states under study, as well as their effect on skin properties, are presented in Table 3.

A description of the diagnostic criteria for all classes and some examples of microscopic images of the mice skin with different types of hyperplasia, were presented in [40]. An example of the AF spectral curves for excitation wavelength $\lambda = 360$ nm obtained for all classes at $SDS_1 = 271$ μm are shown in Figure 2. In addition, Figure 2 shows the standard deviations obtained by averaging the spectra by class.

It can be seen that for all of these classes the areas of standard deviations overlap significantly, making the classification of the spectra a rather difficult task. This problem can be dealt with by implementing data processing techniques in combination with machine learning methods for classification.

## 2.3 | Spectrum analysis pipeline

The general scheme of the spectroscopic data analysis pipeline includes pre-processing, classification and data fusion steps, due to the use of two modalities (DR and AF), seven "submodalities" ($AF_1$–$AF_7$) and three SDS values, which resulted in 24 groups of spectra under study: one DR spectra and seven AF spectra with different excitation wavelengths for each of all three SDS.

### 2.3.1 | Preprocessing of the spectra

The initial spectra preprocessing stage consists of two steps: dimensionality reduction/feature extraction for every group of spectra and normalization. The PCA was

**TABLE 3** Symptoms of the skin states under study and their effects on skin properties.

| Diagnosis | Main symptoms | Cause | Layer of skin |
|---|---|---|---|
| CH | Hyperproliferation of keratinocytes | Increased epidermis thickness | Epidermis |
| AH | Cytological dysmaturation, disorganization of cell layers | Local changes in cell morphology | Epidermis |
| D | Disorganization of cell layers, Dyskeratosis, Parakeratosis, Elastosis | Keratinization, extensive change of a layer organization in the epidermis | Epidermis, dermis (elastosis only) |

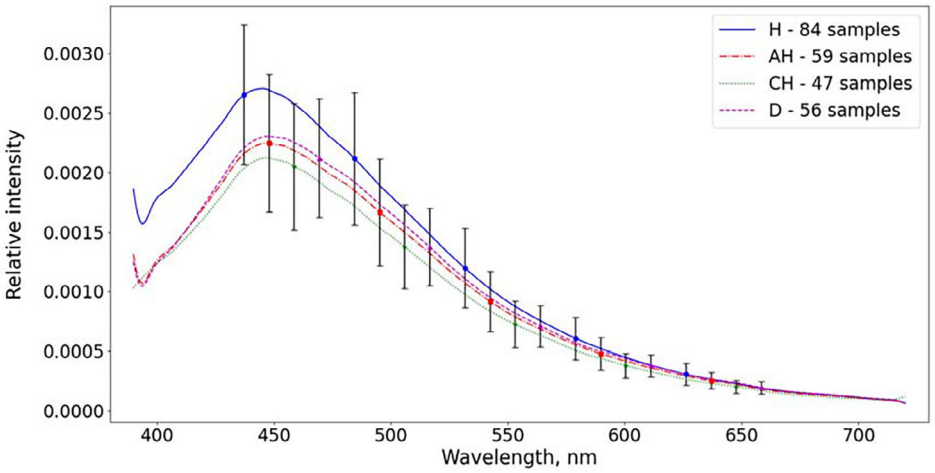


**FIGURE 2** Average AF spectra obtained with excitation wavelength $AF_1 = 360$ nm measured at $SDS_1 = 271$ μm with standard deviations for healthy skin (84 samples), atypical Hyperplasia (59 samples), compensatory hyperplasia (47 samples), and dysplasia (56 samples).

used for feature extraction [39–41]. However, unlike the previous studies, the PCA was applied to each of the initial spectra rather than to a set of manually extracted spectral features. The number of principal components in each case ranged from 2 to 50. It is important to note that the new features derived from PCA are uncorrelated, which is particularly important for further classification step. In addition, several kernels were tested for PCA: linear, polynomial, and radial basis function (RBF).

StandardScaler and MinMaxScaler functions were proposed as normalization methods. It should be also noted that the final result of the classification can be influenced not only by the method of normalization, but also by the stage at which it is implemented. To find the best combination of normalization method and stage of its application, all the normalization methods were applied before and after the application of PCA. The corresponding equations for StandardScaler (1) and MinMaxScaler (2) are shown as follows:

$$X_{\mathrm{StSc}} = \frac{X - X_{\mathrm{mean}}}{X_{\mathrm{std}}} \quad (1)$$

where $X$ is the variable, $X_{\mathrm{StSc}}$ is the value of the variable after applying StandardScaler, $X_{\mathrm{mean}}$ is the mean value of the variable $X$ and $X_{\mathrm{std}}$ is the standard deviation of $X$,

$$X_{\mathrm{MinMax}} = \frac{X - X_{\mathrm{min}}}{X_{\mathrm{max}} - X_{\mathrm{min}}} \quad (2)$$

where $X_{\mathrm{MinMax}}$ is the value of the variable after applying MinMaxScaler, $X_{\mathrm{min}}$ is the minimum value of $X$, and $X_{\mathrm{max}}$ is the maximal value of $X$.

### 2.3.2 | Classification of the spectra

After dimensionality reduction step, classification of the spectra with the optimization of hyperparameters for each classifier was carried out using SVM [43], MLPC [44], LDA [45], and RF [46]. All classifiers were tested in parallel in order to select the most accurate one and corresponding set of hyperparameters. For SVM, which is a binary classifier, different approaches have been also tested for multiclass classification: one-vs.-one (OVO) classification when each class is opposed to each class, after which the results of all binary classifications are also summarized and one-vs.-rest (OVR) when each class is compared to a combination of all other classes in turn, and then the results are generalized. A list of hyperparameters is given in the Table 4.

A stratified $k$-fold cross validation (CV) [47] was used to evaluate the classification performance. The $k$-value was varied from 3 up to 20 in order to find the

**TABLE 4** List of classification methods and corresponding hyperparameters.

| Name of the method | List of optimized hyperparameters | Variation of the hyperparameters |
|---|---|---|
| Support vector machine (SVM) | Kernel | Linear/Polynomial (2,3)/RBF |
| | Regularization parameter value | 0.1–10 |
| | Decision function type | OVO/OVR |
| Multi-layered perceptron (MLPC) | Number of hidden layers | 1–4 |
| | Size of each hidden layer | 10–100 |
| | Type of the activation function | Identity/logistic/ rectified linear unit (ReLU) |
| Linear discriminant analysis (LDA) | Type of solver | SVD/LSQR |
| Random forest (RF) | Number of trees | 10–150 |

optimal value. In addition, leave-one-out cross validation (LOOCV) [47] was performed when SVM and LDA were used for classification.

The evaluation of the effectiveness of classification was based on two quality criteria: the multiclass classification accuracy (Equation 3) and the error in classifying precancerous lesions as healthy (Equation 4):

$$\mathrm{Acc} = \frac{\mathrm{TP_{CH}} + \mathrm{TP_{AH}} + \mathrm{TP_D} + \mathrm{TP_H}}{N_\mathrm{T}} \times 100\%, \quad (3)$$

where $\mathrm{TP}_i$ stands for correctly classified results for class $i$ and $N_\mathrm{T}$ refers to as the total number of samples.

$$\mathrm{Err} = \frac{\mathrm{FP_{AH-H}} + \mathrm{FP_{AH-CH}} + \mathrm{FP_{D-H}} + \mathrm{FP_{D-CH}}}{N_\mathrm{AH} + N_\mathrm{D}} \times 100\%, \quad (4)$$

where $\mathrm{FP}_{i-j}$ represents misclassified results corresponding to class $i$ incorrectly predicted as class $j$ and $N_i$ is the number of samples for class $i$.

The general scheme of spectra classification is shown in Figure 3.

## 2.4 | Data fusion

The fusion of information from all the AF and DR spectra was carried out by analyzing the results of the classification of every of 24 groups of spectra. This approach is also called decision fusion. The most standard method used for decision fusion is majority voting. However, when using majority voting it is not possible to take into account differences in the accuracy of the original predictions, which may have a negative impact on the final result. To avoid this problem, two other methods were tested to combine the decisions in parallel with majority voting: stacking and manual optimization of weights (MO).

Another important point is that the different accuracy of the predictions for all 24 groups of spectra, as well as the correlation between them, leads to the fact that using all the data at once can also reduce the final classification accuracy. For this reason, the data were combined in three ways: combining all groups of spectra at once (1 result), by modality/submodality of the spectra (8 results) and by their SDS (3 results). In addition, for the last two cases, decision fusion was repeated again for the new predictions obtained.

The general scheme for MO (Figure 4) includes calculation of the weights ($w_i$) for each selected group of spectra, following by the aggregation of the contributions of all groups to the final diagnosis for each sample (Σ). The weights were changed for all groups and their combinations from 0 to 1 in steps of 0.1 after normalization of their values to make the sum of the weights equal to 1. After summing up the contributions from each group of spectra, a prediction was generated and the accuracy of the prediction was then evaluated. If the classification accuracy was lower than the best value obtained earlier (or the error value was higher when the accuracy was equal), the values of the weights were changed. The process was stopped after going through all the values of weights.

The general scheme of stacking which involves adding one more classifier that is used do analyze decisions obtained by the first step of classification as new set of features, is shown on Figure 5. The classification and optimization strategy is similar to the one described in Section 3.2.

# 3 | RESULTS AND DISCUSSION

## 3.1 | Optimization of hyperparameters for preprocessing and classification steps

The process of optimizing the hyperparameters was carried out based on the accuracy of the classification. The first step involved the selection of an optimal number of principal components used in the study, as well as the selection of the kernel for PCA, that provide the best accuracy of classification.

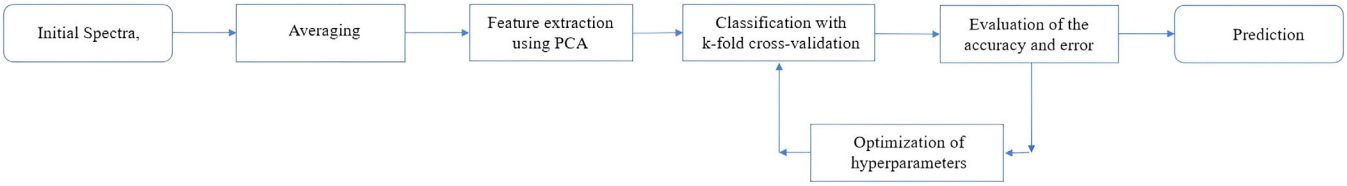


**FIGURE 3** The main scheme of spectra classification.

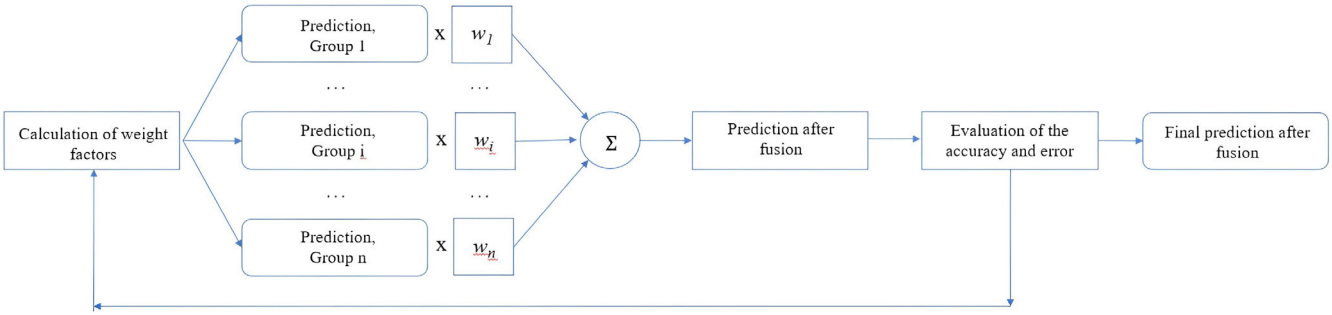


**FIGURE 4** The main scheme of data analysis by using manual optimization of weights.

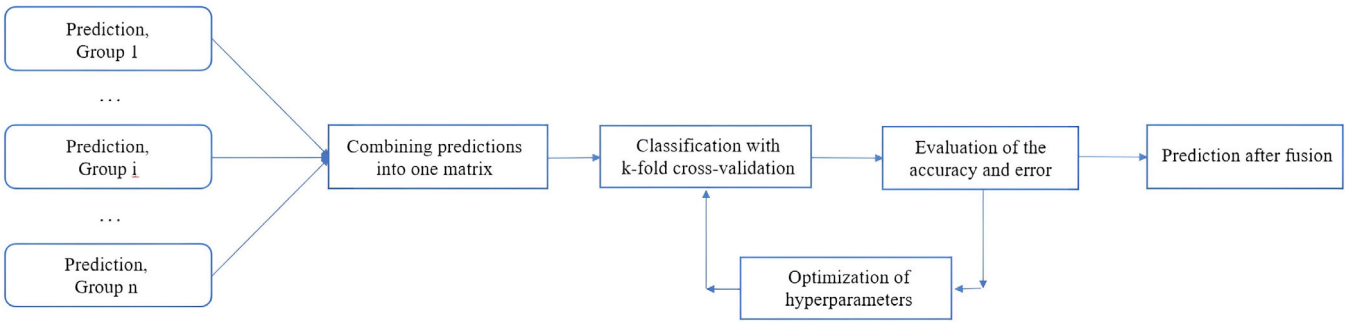


**FIGURE 5** The main scheme of data analysis by using stacking.

An example of a 3D distribution of the thirst three principal components for DR spectra (SDS = 536 μm) for all the classes is shown on Figure 6.

It can be seen that the point clouds corresponding to each class are overlapped. This result is repeated for all other modalities/submodalities and SDS, consequently, no visual separation between all classes could be achieved. The use of other combinations of principal components also did not provide any effect, therefore it was decided to use a larger number of principal components for the classification. An example of the dependency between the accuracy of multi-class classification using SVMs and the number of principal components (from 2 to 80) for DR spectra obtained at $SDS_2$ is shown in Figure 7.

It can be seen that when the number of principal components used for classification is higher than 20, the accuracy of the multiclass classification reaches a ceiling value of about 90%. This correlation was the same for all groups of spectra, but the number of principal components used for classification, for which the max constant value of accuracy was reached, varied between 20 and 30. In addition, no improvement in efficiency of classification was achieved by varying the kernels. Therefore, the PCA was implemented using linear kernel in all cases.

The use of different kernels for the SVM also provided very similar results, so the kernels that required less computation time were used for spectrum classification (linear kernel and RBF kernel). A similar approach was used to choose the optimal hyperparameters for the classifiers used.

The last step of optimization was to find the optimal cross-validation method (LOOCV/*k*-fold CV) and the optimal value of the *k* parameter (for *k*-fold CV) which provided an optimal balance between the resulting accuracy and computation time. For this purpose, the value of

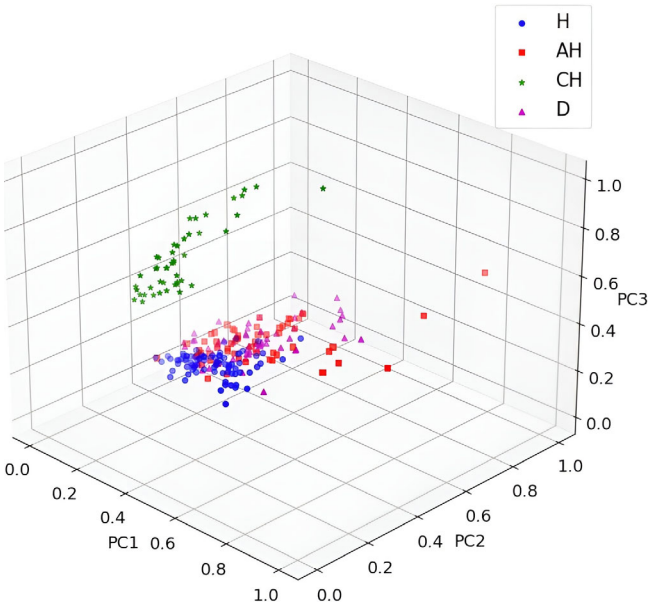


FIGURE 6 3D distribution of the first three principal components for all four classes of spectra.

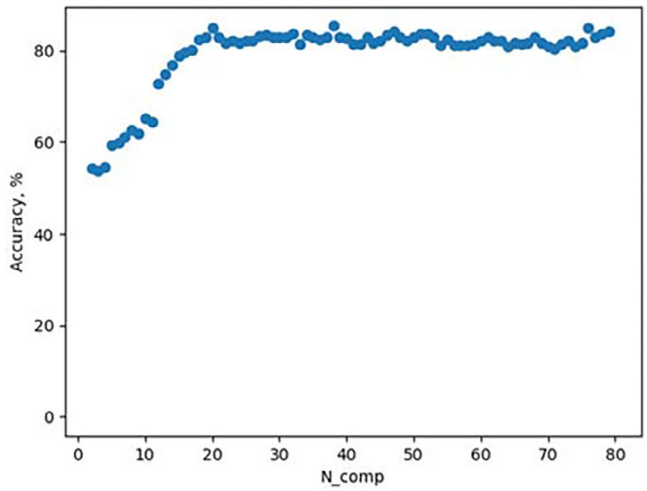


FIGURE 7 Dependence of the classification accuracy on the number of principal components used.

parameter $k$ was varied from 4 to 20 for all groups of spectra. SVM (with linear and RBF kernels) and LDA were used as classifiers, with only the most accurate result selected for further analysis. The number of principal components used after PCA was equal to 25 in all cases. For almost all groups of spectra, the difference between the minimum and maximum values of the multiclass classification accuracy was less than 2.5%. For further calculations, the value of k was chosen to be 8, since the classification results corresponding to this value were maximal or close to it for all groups of spectra. In addition, it does not require a long computation time, compared to LOOCV.

TABLE 5 Optimization of hyperparameters for methods used.

| Name of the method | List of optimized hyperparameters | Optimized hyperparameters |
|---|---|---|
| Principal component analysis (PCA) | Number of PCs | 25 |
| | Kernel | Linear |
| Support vector machine (SVM) | Kernel | Linear/ RBF |
| | Regularization parameter value | 1 |
| | Decision function type | OVO |
| Multi-layered perceptron (MLPC) | Number of hidden layers | 1 |
| | Size of each hidden layer | 80 |
| | Type of the activation function | ReLU |
| Linear discriminant analysis (LDA) | Type of solver | SVD |
| Random forest (RF) | Number of trees | 100 |

The results of the optimization are presented in Table 5. The use of more than one hyperparameter value/option in the table means that the values of multiclass classification accuracy obtained in the corresponding cases differed by no more than 1%, and the required computation time differed by no more than 10 s.

## 3.2 | Results of classification for different groups of spectra

The classification of each of the 24 groups of spectra was done by all methods in parallel and a classifier with the best performance were chosen for each group of spectra. All calculations were repeated 5 times to get statistically relevant results. Average accuracy values obtained by the different classifiers (SVM, MLPC, DA, and RBF) for all modalities (DR and all AF) and all SDS are shown in Figure 8 (for sake of clarity, error bars are plotted only for standard deviation values greater than 1%).

It can be seen that all the classification methods used, except RF, showed very similar accuracy in most cases. It can also be noted that for all SDS, the best results were obtained for the classification of DR spectra. The multiclass classification accuracy and percentage of potentially precancerous lesions classified as healthy are presented in Table 6 for all groups of spectra.

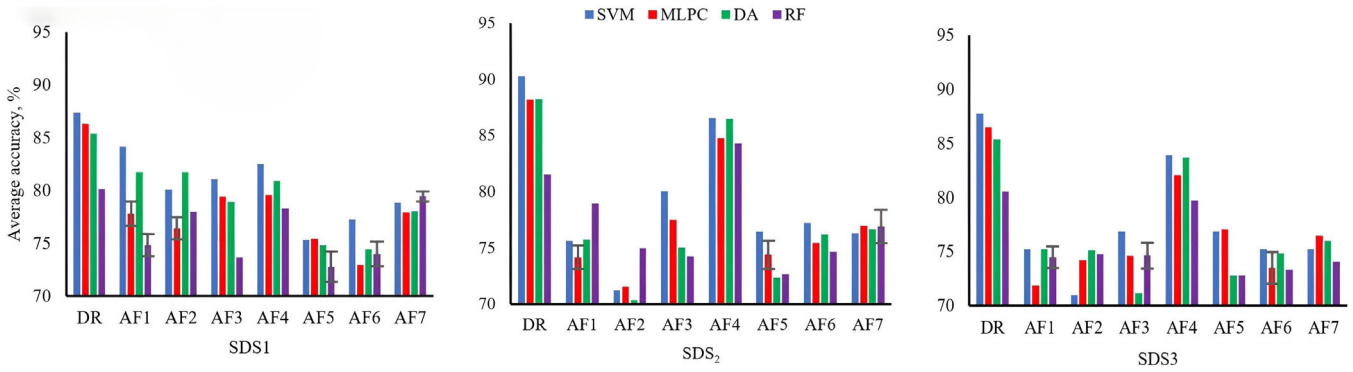


**FIGURE 8** Average classification accuracy obtained by different classifiers (SVM, MLPC, DA, and RBF) for all modalities (DR and all AF) and all SDS; error bars indicate standard deviation (SD) values corresponding to five repeated calculations for each combination of source, detector and classifier (error bars not shown for SD < 1%).

**TABLE 6** Values of accuracy and misclassification for PP states for all modalities and sub-modalities.

| | $SDS_1 = 271$ µm | | $SDS_2 = 536$ µm | | $SDS_3 = 834$ µm | |
|---|---|---|---|---|---|---|
| **Group of spectra** | **Acc. (%)** | **Err. (%)** | **Acc. (%)** | **Err. (%)** | **Acc. (%)** | **Err. (%)** |
| DR | 87.40 | 4.35 | **90.24** | **0.87** | 86.99 | 6.09 |
| $AF_1$ | **84.15** | **6.96** | 78.05 | 12.17 | 76.42 | 14.78 |
| $AF_2$ | 81.71 | 6.96 | 75.20 | 14.78 | 77.24 | 21.24 |
| $AF_3$ | 81.30 | 6.96 | 78.05 | 10.43 | 77.64 | 13.04 |
| $AF_4$ | 82.52 | 11.30 | **86.59** | **6.09** | 83.33 | 7.73 |
| $AF_5$ | 77.24 | 12.17 | 78.46 | 13.91 | 76.02 | 11.30 |
| $AF_6$ | 75.61 | 19.13 | 77.64 | 11.30 | 73.98 | 24.35 |
| $AF_7$ | 79.27 | 13.91 | 79.27 | 13.91 | 77.24 | 19.13 |

*Note*: The best results for different modalities or ways of combining the data are in bold.

For a more detailed analysis, two best results were selected for each SDS. The corresponding confusion matrices are presented in Table 7.

It can be seen that for all three values of SDS the highest multiclass classification accuracy (90.24%) and lowest value of error in classification of PP states (0.87%) were obtained for DR spectra, which is a significant improvement compared to the results obtained in the previous studies [39–41]. This may be explained by the fact that the implementation of PCA for feature extraction without preliminary step of feature selection provides greater efficiency in extracting important information from the initial DR spectra which is also indirectly confirmed by the fact that the classification accuracy of the AF spectra has also increased compared to the same studies [39–41]. According to histological criteria, higher classification accuracy of DR spectra may relate both to a change in the absorption properties of the skin with PP states due to keratosis, and scattering properties of the skin with PP lesions, due to disorganization of the cell layers.

Among the different SDS values, the best results for AF spectra (Acc = 84.15%, Err = 6.96%) with excitation wavelengths $\lambda < 400$ nm were obtained for $SDS_1 = 271$ µm. This may be due to the fact that these wavelengths have a lower penetration depth into the skin, which affects the quality of the spectra obtained for larger SDS values. In addition, according to histological classification criteria, most of the changes in skin properties due to lesions are related with changes in the concentration of keratin, which has a fluorescence excitation peak in the 380–400 nm range [25]. Also in cases of dysplasia, degradation of collagen and elastin in the dermis can affect the final accuracy of the classification, as collagen, elastin, and their cross-links also have fluorescence excitation peaks in the 360–400 nm range.

However, the best results for DR spectra (Acc = 90.24%, Err = 0.87%) and AF spectra with an excitation wavelength of $\lambda \geq 400$ nm (Acc = 86.59%, Err = 6.09%) were obtained for $SDS_2 = 536$ µm. It can be explained by the fact that this value of SDS provides the optimal balance between the penetration depth into the skin and the proportion of noise in the signal, as increasing SDS increases the contribution of the signal received from the deeper layers of the skin (including the dermis) to the resulting

**TABLE 7** Confusion matrices corresponding to the most accurate results for every SDS.

| $SDS_1 = 271$ µm | | | | | | | | | |
|---|---|---|---|---|---|---|---|---|---|
| **DR** | | | | | **$AF_1$** | | | | |
| | **AH** | **CH** | **D** | **H** | | **AH** | **CH** | **D** | **H** |
| AH | 71.19 | 0 | 23.73 | 5.08 | AH | 66.10 | 0 | 22.03 | 11.86 |
| CH | 2.13 | 95.74 | 2.13 | 0 | CH | 0 | 100 | 0 | 0 |
| D | 17.86 | 0 | 78.57 | 3.57 | D | 28.57 | 0 | 69.64 | 1.79 |
| H | 0 | 0 | 0 | 100 | H | 2.38 | 0 | 0 | 97.62 |
| **$SDS_2 = 536$ µm** | | | | | | | | | |
| **DR** | | | | | **$AF_4$** | | | | |
| | **AH** | **CH** | **D** | **H** | | **AH** | **CH** | **D** | **H** |
| AH | 88.14 | 0 | 10.17 | 1.69 | AH | 74.58 | 0 | 16.95 | 8.47 |
| CH | 0 | 93.62 | 2.13 | 4.26 | CH | 0 | 100 | 0 | 0 |
| D | 21.43 | 0 | 78.57 | 0 | D | 19.64 | 0 | 76.79 | 3.57 |
| H | 2.38 | 0 | 0 | 97.62 | H | 2.38 | 0 | 3.57 | 94.05 |
| **$SDS_3 = 834$ µm** | | | | | | | | | |
| **DR** | | | | | **$AF_4$** | | | | |
| **DR** | **AH** | **CH** | **D** | **H** | | **AH** | **CH** | **D** | **H** |
| AH | 67.80 | 0 | 23.73 | 8.47 | AH | 66.10 | 0 | 20.34 | 13.56 |
| CH | 0 | 100 | 0 | 0 | CH | 2.13 | 95.74 | 2.13 | 0 |
| D | 17.86 | 0 | 78.57 | 3.57 | D | 26.79 | 0 | 71.43 | 1.79 |
| H | 0 | 0 | 1.19 | 98.81 | H | 3.57 | 0 | 0 | 96.43 |

spectrum. Moreover, the results obtained for the DR spectra collected at $SDS_2$ are the best of all the results obtained in this step. Consequently, this suggests significantly changes of scattering properties of skin layers (including the dermis) related to their morphological and structural modifications.

It can also be noticed that in all cases, the precision values of classification of benign classes (H and CH) ranges from 93% to 100%, while the precision values of classification of PP states ranges from 66% to 88%. At the same time for the best result presented (DR spectra for $SDS_2$), only 1.69% of all samples corresponding to atypical hyperplasia were classified as healthy, whereas for dysplasia there were no such samples at all. Thus, the number of samples corresponding to potentially precancerous skin states that were classified as benign or healthy was 0.8% of all samples that belong to PP classes according to the reference classification. In order to improve this result, all spectra were redivided into two groups, PP and benign and then spectra processing pipeline was repeated. The results presented in Table 8. All results presented are consistent with the classification of the DR spectra, as in the case of multiclass classification, the best results were obtained for it among both modalities and all groups of spectra.

It can be seen that in case of binary classification for spectra obtained at $SDS_1$ the proportion of PP classified as benign is 0. For $SDS_2$ and $SDS_3$ the obtained coefficients of the confusion matrices are very similar.

## 3.3 | Application of data fusion methods

The next step was to combine the results from the different groups of spectra by fusion of decisions in three ways: fusion of decisions for all groups of spectra, fusion of decisions according to the initial spectra modality or excitation wavelength value (for AF spectra), and fusion of decision according to SDS of the initial spectra. All results are presented in Tables 9–11, respectively.

It can be noted that, in most cases, implementation of MO provides the best results among all three methods for both evaluated parameters. It can be explained by the influence of overfitting in case of stacking and the lack of corrections for the difference in classification efficiency based on different groups of spectra in case of MV.

**TABLE 8** Results of binary classification obtained using DR spectra for every SDS.

| $SDS_1$ | | | $SDS_2$ | | | $SDS_3$ | | |
|---|---|---|---|---|---|---|---|---|
| | **Benign** | **PP** | | **Benign** | **PP** | | **Benign** | **PP** |
| Benign | 93.13 | 6.87 | Benign | 95.42 | 4.58 | Benign | 96.18 | 3.82 |
| PP | 0 | 100 | PP | 1.74 | 98.26 | PP | 1.74 | 98.26 |

**TABLE 9** Results obtained by using decision fusion for modalities/sub-modalities.

| | **Majority voting** | | **Stacking** | | **Manual optimization of weights** | |
|---|---|---|---|---|---|---|
| **Groups of spectra for fusion** | **Acc. (%)** | **Err. (%)** | **Acc. (%)** | **Err. (%)** | **Acc. (%)** | **Err. (%)** |
| All groups | **89.02** | **3.48** | 86.59 | 7.83 | – | – |
| DR | 89.84 | 1.74 | **90.24** | 1.74 | **90.24** | **0.87** |
| $AF_1$ | 80.49 | 4.35 | 84.15 | 8.70 | 84.96 | 6.96 |
| $AF_2$ | 80.08 | 8.70 | 80.08 | 15.65 | 81.71 | 6.96 |
| $AF_3$ | 79.27 | 4.35 | 82.52 | 12.71 | 83.33 | 9.57 |
| $AF_4$ | 86.99 | 6.96 | 87.80 | 7.83 | **89.02** | **5.22** |
| $AF_5$ | 76.02 | 10.43 | 80.08 | 12.71 | 83.30 | 9.57 |
| $AF_6$ | 73.58 | 17.39 | 79.67 | 17.39 | 80.08 | 14.78 |
| $AF_7$ | 78.46 | 15.65 | 80.49 | 19.13 | 82.11 | 13.04 |
| All DR and AF (step 2) | 87.80 | 4.35 | 85.77 | 11.30 | **93.90** | **1.74** |

*Note*: The best results for different modalities or ways of combining the data are in bold.

**TABLE 10** Classification results for all spectra after two steps of decision fusion.

| **DR** | **AH** | **CH** | **D** | **H** |
|---|---|---|---|---|
| AH | 91.53 | 0 | 5.08 | 3.39 |
| CH | 0 | 100 | 0 | 0 |
| D | 17.86 | 0 | 82.14 | 0 |
| H | 0 | 0 | 0 | 100 |

In addition, as in the previous case, the selection of the best result was based on the multiclass classification accuracy. However, the use of MO requires a much longer computation time.

Figure 9 shows the average accuracy ± SD bar graphs allowing to compare the performance of the different classifiers (SVM, MLPC, LDA, and RF) for different strategy of combining/choosing data for decision fusion by stacking. It can be seen that Random Forest and SVM provided the best performance in most cases.

The best results of decision fusion, as for the separate classification, were obtained for DR spectra and AF spectra with excitation wavelength of $\lambda = 400$ nm. In case of the DR spectra, the confusion matrix coefficients were identical to the ones presented in Table 4c, which correspond to the classification results based on DR spectra for $SDS_2 = 536$ μm. The use of decision fusion for the AF spectra gives an average improvement of 3%–5% in multiclass classification accuracy.

The best results for fusion of decisions by group of spectra, that were obtained by using two steps of manual optimization of weights are presented in Table 10.

It can be seen that the precision values for all classes increased by 5%–7% and reached 100% for benign states compared to the results presented in Table 7. At the same time, the error in classification of atypical hyperplasia as healthy tissue also increased. This was due to the fact that the selection of the best combination of coefficients for MO was based on the multiclass classification accuracy.

When combining the SDS classification results, the best results (Acc = 94.31%, Err = 0.87%) were obtained for $SDS_2 = 536$ μm, as in the previous case. The corresponding results that were obtained by using MO are presented in Table 12.

Compared to the results presented in Table 7, the value of precision for all classes also increased by 5%–7% and reached 100% for benign states, as in the case of decision fusion by modality. The use of MO and stacking for decision fusion by SDS value increased the multiclass classification accuracy by 2%–4%. At the same time, additional step of decision fusion produced no improvement with respect to the result obtained for $SDS_2 = 536$ μm.

**TABLE 11** Results of decision fusion by SDS.

| | Majority voting | | Stacking | | Manual optimization of weights | |
|---|---|---|---|---|---|---|
| **Distance** | **Acc. (%)** | **Err. (%)** | **Acc. (%)** | **Err. (%)** | **Acc. (%)** | **Err. (%)** |
| $SDS_1$ | 86.18 | 7.83 | 86.18 | 3.48 | 90.24 | 5.22 |
| $SDS_2$ | 88.21 | 10.43 | **92.68** | **1.74** | **94.31** | **0.87** |
| $SDS_3$ | 82.52 | 13.91 | 85.37 | 6.96 | 89.43 | 6.09 |
| Final 2 | 86.59 | 9.57 | 91.06 | 4.35 | **94.31** | **0.87** |

*Note*: The best results for different modalities or ways of combining the data are in bold.

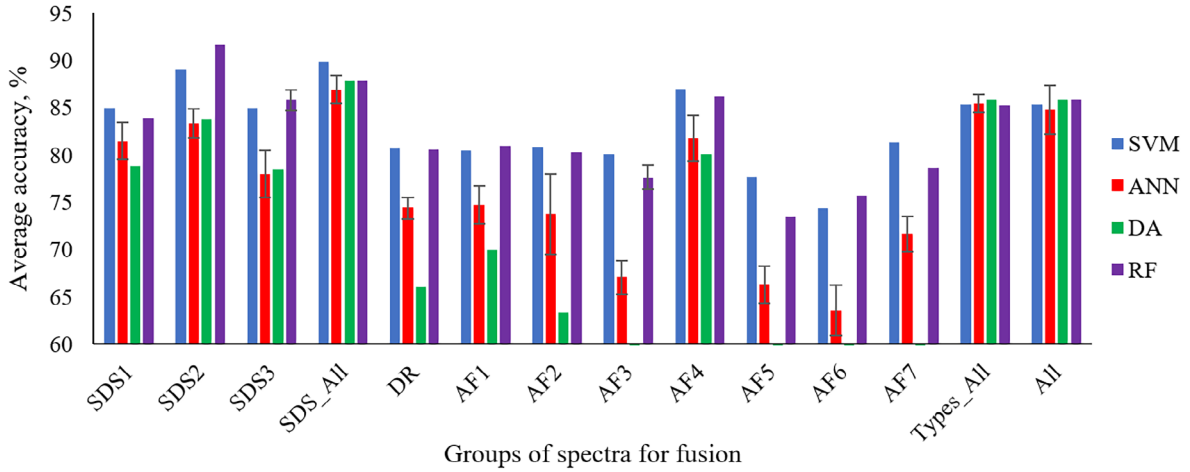


**FIGURE 9** Average accuracy for stacking (decision fusion) obtained by different classifiers (SVM, MLPC, DA, and RBF) for all ways to combine data (by SDS, by modality and all data at once); error bars indicate SD values corresponding to five repeated calculations for each combination of source, detector and classifier (error bars not shown for SD < 1%).

**TABLE 12** Classification results (confusion matrix) based on decisions obtained from all types of spectra.

| | AH | CH | D | H |
|---|---|---|---|---|
| AH | 91.53 | 0 | 6.78 | 1.69 |
| CH | 0 | 100 | 0 | 0 |
| D | 16.07 | 0 | 83.93 | 0 |
| H | 0 | 0 | 0 | 100 |

For the case of binary classification, the fusion of decisions was done in the same way as for multi-class classification. The best results (for fusion of the second decision fusion step) are presented in Table 13 for distances (a) and groups of spectra (b).

It can be noted that the percentage of misclassifying the PP state as healthy is less than 1%. Moreover, the resulting error is most likely the result of statistical error due to the use of cross-validation. At the same time, the corresponding value of precision, compared to the results obtained without decision fusion, has increased and is close to 100%.

**TABLE 13** Results of decision fusion for binary classification.

| | Benign | PP |
|---|---|---|
| $SDS_1$ | | |
| Benign | 100 | 0 |
| PP | 0.87 | 99.13 |
| $SDS_3$ | | |
| Benign | 99.24 | 0.76 |
| PP | 0.87 | 99.13 |

## 4 | CONCLUSION

This study presents a developed and tested pipeline for the classification of multimodal spectroscopic data obtained from benign and precancerous skin lesions, which includes the use of feature extraction, machine learning and data fusion methods. The implementation of this pipeline allowed a significant increase of the accuracy of multiclass classification of these lesions compared to previous studies.

The spectra corresponding to each group of spectra were processed separately, followed by a one- or two-step decision analysis. The feature extraction was made by using PCA, after which the spectra were classified using support vector machine, multilayer perceptron, linear discriminant analysis, and random forest. The next step was to use data fusion, which was done in three ways: combining all results at once, combining all groups of spectra by corresponding distances, followed by combining the results, and combining all groups of spectra by modality, also followed by combining into one final result.

The highest accuracy of the multiclass classification was achieved using support vector machine for the first step of classification and manual optimization of weights to combine all types of spectra corresponding to $SDS_2 = 536$ μm for the second step of classification and was 94.41%. It can be explained by the fact that this value of SDS provides an optimal balance between depth of penetration into the skin and the proportion of noise in the signal.

Among the different spectral types, the highest classification accuracy was obtained for the DR spectra for all SDS. This observation can be explained by the fact that for the whole spectral range the DR spectra are equally affected by the absorption properties of internal skin components range as well as by scattering properties, which are influenced by pathological states of the skin. However, this fact cannot be clearly confirmed by the list of methods used in our study. This issue should be investigated in the following articles.

## ACKNOWLEDGMENTS

The research was carried out with the support of a PhD grant under Vernadski international joint PhD program (2021–2024) provided by the French embassy in the Russian Federation complemented by the University of Lorraine, and a grant under the Decree of the Government of the Russian Federation No. 220 of April 9, 2010 (Agreement No. 075-15-2021-615 of June 4, 2021).

## CONFLICT OF INTEREST STATEMENT

The authors declare no financial or commercial conflict of interest.

## DATA AVAILABILITY STATEMENT

The data that support the findings of this study are available from the any of authors upon reasonable request.

## ORCID

*Valentin Kupriyanov* https://orcid.org/0000-0002-1072-0170
*Walter Blondel* https://orcid.org/0000-0001-5866-7228
*Yury Kistenev* https://orcid.org/0000-0001-5760-1462

## REFERENCES

[1] C. F. Heal, B. A. Raasch, P. G. Buettner, D. B. Weedon, *J. Dermatol.* **2008**, *159*, 661.
[2] T. M. Jørgensen, A. Tycho, M. Mogensen, P. Bjerring, G. B. Jemec, *Skin Res. Technol.* **2008**, *14*, 364.
[3] T. Hinz, L. K. Ehler, H. Voth, I. Fortmeier, T. Hoeller, T. Hornung, M. H. Schmid-Wendtner, *Dermatology* **2011**, *223*, 161.
[4] A. Dubois, O. Levecq, H. Azimani, D. Siret, A. Barut, M. Suppa, V. Del Marmol, J. Malvehy, E. Cinotti, P. Rubegni, J. L. Perrot, *J. Biomed. Opt.* **2018**, *23*, 106007.
[5] D. S. Gareau, J. K. Karen, S. W. Dusza, M. Tudisco, K. S. Nehal, M. Rajadhyaksha, *J. Biomed. Opt.* **2009**, *14*, 034012.
[6] F. Farnetani, A. Scope, R. P. Braun, S. Gonzalez, P. Guitera, J. Malvehy, M. Manfredini, A. A. Marghoob, E. Moscarella, M. Oliviero, S. Puig, H. S. Rabinovitz, I. Stanganelli, C. Longo, C. Malagoli, M. Vinceti, G. Pellacani, *JAMA Dermatol.* **2015**, *151*, 1075.
[7] S. Segura, S. Puig, C. Carrera, J. Palou, J. Malvehy, *J. Am. Acad. Dermatol.* **2009**, *61*, 216.
[8] R. Leon, B. Martinez-Vega, H. Fabelo, S. Ortega, V. Melian, I. Castaño, et al., *J. Clin. Med.* **2020**, *9*, 1662.
[9] L. A. Courtenay, D. González-Aguilera, S. Lagüela, S. Del Pozo, C. Ruiz-Mendez, I. Barbero-García, C. Román-Curto, J. Cañueto, C. Santos-Durán, M. E. Cardeñoso-Álvarez, M. Roncero-Riesco, D. Hernandez-Lopez, D. Guerrero-Sevilla, P. Rodríguez-Gonzalvez, *Biomed. Opt. Express* **2021**, *12*, 5107.
[10] A. Pardo, J. A. Gutiérrez-Gutiérrez, I. Lihacova, J. M. López-Higuera, O. M. Conde, *Biomed. Opt. Express* **2018**, *9*, 6283.
[11] S. Tomatis, A. Bono, C. Bartoli, M. Carrara, M. Lualdi, G. Tragni, R. Marchesini, *Med. Phys.* **2003**, *30*, 212.
[12] M. Carrara, A. Bono, C. Bartoli, A. Colombo, M. Lualdi, D. Moglia, et al., *Phys. Med. Biol.* **2007**, *52*, 2599.
[13] A. M. F. Lima, C. R. Daniel, R. S. Navarro, B. Bodanese, C. A. Pasqualucci, M. T. T. Pacheco, R. A. Zangaro, L. Silveira Jr., *Vib. Spectrosc.* **2019**, *100*, 131.
[14] S. Sigurdsson, P. A. Philipsen, L. K. Hansen, J. Larsen, M. Gniadecka, H. C. Wulf, *IEEE Trans. Biomed. Eng.* **2004**, *51*, 1784.
[15] M. Gniadecka, P. A. Philipsen, S. Wessel, R. Gniadecki, H. C. Wulf, S. Sigurdsson, O. F. Nielsen, D. H. Christensen, J. Hercogova, K. Rossen, H. K. Thomsen, L. K. Hansen, *J. Invest. Dermatol.* **2004**, *122*, 443.
[16] C. A. Lieber, S. K. Majumder, D. D. Billheimer, D. L. Ellis, A. Mahadevan-Jansen, *J. Biomed. Opt.* **2009**, *13*, 024013.
[17] Ł. Szyc, U. Hillen, C. Scharlach, F. Kauer, C. Garbe, *Diagnostics* **2019**, *9*, 103.
[18] M. Panjehpour, C. E. Julius, M. N. Phan, T. Vo-Dinh, S. Overholt, *Lasers Surg. Med.* **2002**, *31*, 367.
[19] B. W. Chwirot, N. Sypniewska, Z. Michniewicz, J. Redzinski, S. Chwirot, G. Kurzawski, W. Ruka, *J. Invest. Dermatol.* **2001**, *117*, 1449.
[20] M. H. Nguyen, Y. Zhang, F. Wang, J. D. L. G. E. Linan, M. K. Markey, J. W. Tunnell, *J. Biomed. Opt.* **2021**, *26*, 052912.
[21] Y. Zhang, A. J. Moy, X. Feng, H. T. M. Nguyen, K. R. Sebastian, J. S. Reichenberg, M. K. Markey, J. W. Tunnell. Translational Biophotonics. **2020**.
[22] A. Garcia-Uribe, J. Zou, M. Duvic, J. H. Cho-Vega, V. G. Prieto, L. V. Wang, *Cancer Res.* **2012**, *72*, 2738.

[23] A. C. Croce, A. Ferrigno, G. Bottiroli, M. Vairetti, *Liver Int.* **2018**, *38*, 1160.
[24] E. Borisova, P. Pavlova, E. Pavlova, P. Troyanova, L. Avramov, *Int. J. Bioautom.* **2012**, *16*, 53.
[25] E. Borisova, P. Troyanova, P. Pavlova, L. Avramov, *Quantum Electron.* **2008**, *38*, 597.
[26] E. Borisova, E. Pavlova, T. Kundurjiev, P. Troyanova, T. Genova, L. Avramov, *Biophotonics: Photonic Solutions for Better Health Care IV*, Vol. 9129, SPIE Photonics Europe conference, 2014, Brussels, Belgium **2014**, May, p. 251.
[27] N. Rajaram, J. S. Reichenberg, M. R. Migden, T. H. Nguyen, J. W. Tunnell, *Lasers Surg. Med.* **2010**, *42*, 876.
[28] A. J. Thompson, S. Coda, M. B. Sørensen, G. Kennedy, R. Patalay, U. Waitong-Brämming, P. A. A. De Beule, M. A. A. Neil, S. Andersson-Engels, N. Bendsøe, P. M. W. French, K. Svanberg, C. Dunsby, *J. Biophotonics* **2012**, *5*, 240.
[29] L. Lim, B. S. Nichols, M. R. Migden, N. Rajaram, J. Reichenberg, M. K. Markey, M. I. Ross, J. W. Tunnell, *J. Biomed. Opt.* **2014**, *19*, 117003.
[30] A. J. Moy, X. Feng, H. T. Nguyen, Y. Zhang, K. R. Sebastian, J. S. Reichenberg, J. W. Tunnell, *Photon. Dermatol. Plast. Surg.* **2017**, February, *10037*, 21 SPIE.21–26.
[31] Z. M. Hira, D. F. Gillies, *Adv. Bioinforma.* **2015**, *2015*, 2015.
[32] B. Ashok, P. Aruna, *Int. J. Eng. Res. Appl.* **2016**, *6*, 94.
[33] K. I. Zaytsev, K. G. Kudrin, V. E. Karasik, I. V. Reshetov, S. O. Yurchenko, *Appl. Phys. Lett.* **2015**, *106*, 053702.
[34] S. X. Li, Q. Y. Zeng, L. F. Li, Y. J. Zhang, M. M. Wan, Z. M. Liu, H. L. Xiong, Z. Y. Guo, S. H. Liu, *J. Biomed. Opt.* **2013**, *18*, 027008.
[35] I. A. Bratchenko, D. N. Artemyev, O. O. Myakinin, M. G. Vrakova, K. S. Shpuntenko, A. A. Moryatov, S. V. Kozlov, V. P. Zakharov, *J. Biomed. Photon. Eng.* **2015**, *1*, 180.
[36] L. Lenhardt, I. Zeković, T. Dramićanin, M. D. Dramićanin, *Phys. Scr.* **2013**, *2013*, 014057.
[37] I. A. Bratchenko, L. A. Bratchenko, Y. A. Khristoforova, A. A. Moryatov, S. V. Kozlov, V. P. Zakharov, *Comput. Methods Prog. Biomed.* **2022**, *219*, 106755.
[38] H. A. Haenssle, C. Fink, F. Toberer, J. Winkler, W. Stolz, T. Deinlein, R. Hofmann-Wellenhof, A. Lallas, S. Emmert, T. Buhl, M. Zutt, A. Blum, M. S. Abassi, L. Thomas, I. Tromme, P. Tschandl, A. Enk, P. Zukervar, *Ann. Oncol.* **2020**, *31*, 137.
[39] M. Amouroux, G. D. Ayil, W. W. Blondel, G. Bourg-Heckly, A. Leroux, F. H. Guillemin, *J. Biomed. Opt.* **2009**, *14*, 014011.
[40] G. Díaz-Ayil, M. Amouroux, W. C. P. M. Blondel, G. Bourg-Heckly, A. Leroux, F. Guillemin, Y. Granjon, *Eur. Phys. J. Appl. Phys.* **2009**, *47*, 12707.
[41] F. Abdat, M. Amouroux, Y. Guermeur, W. C. P. M. Blondel, *Opt. Express* **2012**, *20*, 228.
[42] F. Castanedo, *Sci. World J.* **2013**, *2013*, 2013.
[43] M. Awad, R. Khanna, *In Efficient learning machines*, Apress, Berkeley, CA **2015**, p. 39.
[44] F. Murtagh, *Neurocomputing* **1991**, *2*, 183.
[45] A. Tharwat, *Int. J. Appl. Pattern Recogn.* **2016**, *3*, 145.
[46] Y. Liu, Y. Wang, J. Zhang, *International Conference on Information Computing and Applications*, Springer, Berlin, Heidelberg **2012**, September, p. 246.
[47] D. R. Roberts, V. Bahn, S. Ciuti, M. S. Boyce, J. Elith, G. Guillera-Arroita, S. Hauenstein, J. J. Lahoz-Monfort, B. Schröder, W. Thuiller, D. I. Warton, B. A. Wintle, F. Hartig, C. F. Dormann, *Ecography* **2017**, *40*, 913.

**How to cite this article:** V. Kupriyanov, W. Blondel, C. Daul, M. Amouroux, Y. Kistenev, *J. Biophotonics* **2023**, e202300035. https://doi.org/10.1002/jbio.202300035